

Physical origin of very-high-energy gamma rays from the low-luminosity active galactic nucleus NGC 4278 and implications for neutrino observations

SHILONG CHEN,¹ ABHISHEK DAS,^{2,3,4} B. THEODORE ZHANG,^{5,6} SHIGEO S. KIMURA,^{7,8} KOHTA MURASE,^{2,3,4,9} AND YUNFENG LIANG¹

¹*Laboratory for Relativistic Astrophysics, Department of Physics, Guangxi University, 530004, Nanning, China*

²*Department of Physics, The Pennsylvania State University, University Park, PA 16802, USA*

³*Department of Astronomy & Astrophysics, The Pennsylvania State University, University Park, PA 16802, USA*

⁴*Center for Multimessenger Astrophysics, Institute for Gravitation and the Cosmos, The Pennsylvania State University, University Park, PA 16802, USA*

⁵*Key Laboratory of Particle Astrophysics and Experimental Physics Division and Computing Center, Institute of High Energy Physics, Chinese Academy of Sciences, 100049 Beijing, China*

⁶*TIANFU Cosmic Ray Research Center, 610213, Chengdu, Sichuan, China*

⁷*Frontier Research Institute for Interdisciplinary Sciences, Tohoku University, Sendai 980-8578, Japan*

⁸*Astronomical Institute, Tohoku University, Sendai 980-8578, Japan*

⁹*Center for Gravitational Physics and Quantum Information, Yukawa Institute for Theoretical Physics, Kyoto University, Kyoto 606-8502, Japan*

ABSTRACT

Relativistic jets in active galactic nuclei (AGNs) are known to accelerate particles to extreme energies, yet the physical origin of very-high-energy (VHE) emission from low-luminosity AGNs (LL AGNs) remains unclear. NGC 4278, a local LLAGN, has recently been identified as a VHE source following detections by LHAASO. In this study, we present a multi-wavelength and multi-messenger analysis to investigate the physical origin of this emission. Swift-XRT monitoring reveals a quasi-quiescent state characterized by a low X-ray flux. Modeling the broadband spectral energy distribution with the leptohadronic code AMES, we find that a standard one-zone synchrotron self-Compton (SSC) model underpredicts the VHE flux by $\sim 70\%$ due to the insufficient target photon density provided by the weak X-ray emission, unless a high Doppler factor ($\delta \gtrsim 5$) is invoked. Alternatively, an external inverse-Compton (EIC) scenario—scattering seed photons from a radiatively inefficient accretion flow (RIAF)—successfully reproduces the broadband spectral energy distribution with a modest jet power and Doppler factor. We further explore the neutrino production within a leptohadronic framework. The predicted muon neutrino event rate is highest in the EIC quiescent model, reaching $N_{\nu_\mu} \sim 0.001$ for a 15-year IceCube observation (assuming 0.1% of the Eddington luminosity is partitioned into high-energy protons). Future multi-messenger observations are essential to unveil the details of the high-energy processes of NGC 4278.

Keywords: High energy astrophysics (739) — Gamma-ray astronomy (628) — Low luminosity active galactic nuclei (2033) — Galaxy jets (601) — Neutrino astronomy (1100)

1. INTRODUCTION

Low-luminosity active galactic nuclei (LL AGNs) represent a major AGN population and are ubiquitous in the Universe (L. C. Ho 1999, 2008; N. M. Nagar et al. 2005). They exhibit a lower bolometric luminosity ($L_{\text{bol}} \sim 10^{38} - 10^{44} \text{ erg s}^{-1}$), relative to their Eddington luminosity (L. C. Ho 2008). Regarding their energy

spectra, LL AGNs lack a prominent big blue bump and Fe K α line, the presence of flat or inverted radio spectra, and weak optical and UV emission (L. C. Ho 1999, 2008). The most plausible explanation for their low luminosity is a combination of low mass accretion rates and low radiative efficiencies, likely stemming from an insufficient gas supply in the host galaxy. Consequently, these systems lack the bright broad line region (BLR) and the optically thick accretion disk found in standard

NGC 4278 is an elliptical galaxy belonging to the LGG 279 group (A. M. Garcia 1993). It is located at a redshift of $z = 0.00216$, with R.A. = 185.03° and Dec. = 29.28° (O. González-Martín et al. 2009). The galaxy hosts a supermassive black hole (SMBH) with a mass of $M_{\text{BH}} = (3.09 \pm 0.58) \times 10^8 M_{\odot}$ (T.-G. Wang & X.-G. Zhang 2003; M. Chiaberge et al. 2005), corresponding to an Eddington luminosity of $L_{\text{Edd}} \simeq 3.9 \times 10^{46} \text{ erg s}^{-1}$. NGC 4278 is accreting at a low rate, with an Eddington ratio of $\lambda_{\text{Edd}} \equiv L_{\text{bol}}/L_{\text{Edd}} \sim 7 \times 10^{-6}$ (G. Younes et al. 2010). While NGC 4278 is also classified as a radio-loud AGN, its radio luminosity is at least two orders of magnitude lower than that of powerful radio-loud AGNs. Based on the measured radio core luminosity, the jet power is estimated to be $P_{\text{jet}} \sim (1 - 2) \times 10^{42} \text{ erg s}^{-1}$ (G. Giovannini et al. 2004; K. W. Cavagnolo et al. 2010; S. Pellegrini et al. 2012).

The first LHAASO catalog reported the detection of 1LHAASO J1219+2915, a new high-latitude TeV source identified with the nearby LL AGN NGC 4278 (Z. Cao et al. 2024a). Detected at a significance of 8.8σ , the source is spatially coincident with NGC 4278 within 0.03° , strongly supporting a physical association (Z. Cao et al. 2024b). This detection is notable as NGC 4278 is a LINER galaxy with no corresponding gamma-ray source in the Fermi-LAT 4FGL-DR4 catalog (S. Abdollahi et al. 2022; J. Ballet et al. 2024). The origin of VHE gamma-rays detected by LHAASO during the flaring state has been explained by the one-zone synchrotron self-Compton (SSC) model (J.-S. Lian et al. 2024; S. Dutta & N. Gupta 2024; Z.-R. Wang et al. 2024). However, the origin of VHE gamma-rays in the quasi-quiescent state remains unclear. Recently, A. Shoji et al. (2025) proposed that these gamma-rays originate from pp interactions of escaped cosmic rays (CRs). In this study, we analyze publicly available X-ray and gamma-ray data from 2024–2025, as well as public neutrino data, and explore their implications for the origin of VHE emission.

This paper is structured as follows: Section 2 presents a detailed analysis of the broadband SED of NGC 4278, including X-ray, gamma-ray, and neutrino data. Section 3 describes our methods and the fitting procedure using a leptohadronic numerical code. The results are presented in Section 4, followed by a discussion and summary in Section 5.

2. MULTI-WAVELENGTH AND MULTI-MESSENGER OBSERVATIONS

2.1. Radio observations

VLBA and VLA observations of NGC 4278 at 5 GHz and 8.4 GHz in 1995 and 2000 reveal a two-sided jet

structure with total flux densities ranging from 95 to 135 mJy (G. Giovannini et al. 2004). Assuming that the observed asymmetry arises from Doppler beaming rather than environmental inhomogeneities, jet kinematics was constrained using arm-length ratio and apparent separation velocity β_{sep} . These measurements yield a Doppler factor of $\delta \sim 2.6 - 2.8$, indicating the jets are mildly relativistic and viewed at a small angle to the line-of-sight. The jet extends approximately 20 mas, corresponding to a physical scale of 1.4 pc. The major axis of N2, one of the largest components within the radio emission region, measures 11.17 mas, which translates to a physical size of 0.81 pc. (G. Giovannini et al. 2004).

2.2. X-ray Analysis

We analyze the Swift-XRT observations of NGC 4278 (Table 5 in the Appendix) using HEASOFT (v6.35.1). Data reduction is performed with `xrtpipeline` (v0.13.7) and `CALDB` (v20240522). Using `xselect`, source events are extracted from a 20-pixel radius circle centered on the position of NGC 4278, while background events are taken from a 30–45 pixel annulus. We generate the corresponding Ancillary Response Files (ARFs) using standard tools. Spectra are fitted in the 0.3–8 keV band using `XSPEC` (v12.15.0) with C-statistics. We apply an absorbed power-law model, fixing the Galactic column density at $N_{\text{H}} = 2.2 \times 10^{20} \text{ cm}^{-2}$ (R. Willingale et al. 2013) and allowing the intrinsic absorption, photon index, and normalization to vary. A joint fit to the dataset yields a photon index of $\Gamma = 2.11$ and an unabsorbed flux of $1.43 \times 10^{-12} \text{ erg cm}^{-2} \text{ s}^{-1}$ in the 0.3–10 keV band. The detailed fitting results are presented in Table 4 in the Appendix. Comparison with archival observations (G. Younes et al. 2010; S. Pellegrini et al. 2012) confirms that the source remained in a quasi-quiescent state during this period.

2.3. GeV Gamma-ray Analysis

Although NGC 4278 is generally faint in GeV gamma-rays, a transient detection (4.3σ) has been reported during the 2021–2022 LHAASO active phase (E. Bronzini et al. 2024). Here, we analyze Fermi-LAT data covering MJD 60310–60796 (Jan 2024 – May 2025) using `Fermi tools` (v2.4.0) and `Fermipy` (v1.4.0) (M. Wood et al. 2017). We selected Pass 8 events (100 MeV–300 GeV) within a 15° ROI centered on the source. Standard cuts (`zenith angle < 90°`, `DATA_QUAL > 0`) and the `P8R3_SOURCE_V3` IRFs were used. The model included Galactic and isotropic diffuse backgrounds alongside 4FGL-DR4 point sources. Parameters for sources within 5° are free, while those for sources between 5° – 10° had only normalization free. The analysis yields $\text{TS} = 8.46$,

falling below the detection threshold ($TS \geq 25$). Consequently, we derive 90% confidence level flux upper limits using the profile likelihood method, which are shown in the SED (Figure 2).

2.4. VHE Gamma-ray Observations

Leveraging the high sensitivity of LHAASO, the LHAASO Collaboration recently reported the detection of the VHE gamma-ray source 1LHAASO J1219+2915, spatially associated with NGC 4278, using data collected between 2021 March 5 and 2023 October 31 (Z. Cao et al. 2024b). Historically, NGC 4278 has been classified as a radio-loud AGN but lacked significant gamma-ray detection in Fermi-LAT catalogs, leading to earlier assumptions that such low-luminosity AGNs might be inefficient particle accelerators at high energies.

The LHAASO analysis modeled the source spectrum using a power-law with attenuation from the Extra-galactic Background Light (EBL). The source exhibits distinct activity states: a flaring state with an integrated luminosity of $L_{0.1-10 \text{ TeV}} \sim 3.0 \times 10^{41} \text{ erg s}^{-1}$, and a quasi-quiescent state with $L_{0.1-10 \text{ TeV}} \sim 4.3 \times 10^{40} \text{ erg s}^{-1}$ (Z. Cao et al. 2024b). X-ray and GeV light curves covering the 2024–2025 epoch are presented in Figure 1. The lack of significant variability in these bands supports the classification of the source as being in a quasi-quiescent state during this period.

2.5. Neutrino Observations

For this work, we perform an unbinned likelihood analysis, following the methodology of previous IceCube point-source searches (IceCube Collaboration 2021; M. Aartsen et al. 2018; R. Abbasi et al. 2022; J. Braun et al. 2008) to evaluate the significance of a potential neutrino signal originating from the direction of NGC 4278. Both time-integrated and time-dependent methods are employed to search for neutrino emission from the source.

We mainly utilize a software `SkyLLH`¹⁰, a Python-based tool to develop such analyses in a telescope-independent framework (C. Bellenghi et al. 2023; R. Abbasi et al. 2021; M. Wolf 2019) to analysis IceCube’s 10 year public data (M. Aartsen et al. 2018). We use the time integration and time dependent methods to search the neutrino signal, respectively. The results are summarized in Table 1. In the time-integrated analysis, although the best-fit value of $n_s = 11.4$ is obtained, the corresponding Test Statistic (TS) is negligibly small. This low TS indicates that the apparent excess is consistent with background fluctuations; thus, no significant

neutrino signal is detected. As a reference, the time-integrated 90% sensitivity of IceCube with a spectral index of 2.0 is approximately $3.7 \times 10^{-13} \text{ TeV}^{-1} \text{s}^{-1} \text{cm}^{-2}$ at 1 TeV (M. G. Aartsen et al. 2020). For the time dependent method, we get an excess of neutrino events that is 2.0, corresponding to the TS of 8.2. The best-fit time was 56704 ± 1.18 (MJD). However, it does not reach the level of a statistically significant detection. Then, we perform trials to search for the neutrino flux upper limit by injecting different numbers of neutrino excess events, leading to a neutrino upper limit flux that is about $8.0 \times 10^{-13} \text{ TeV}^{-1} \text{s}^{-1} \text{cm}^{-2}$ at 1 TeV.

In Figure 2, we summarize the broadband SED of NGC 4278 in both quasi-quiescent and flaring states, including the neutrino sensitivity.

3. PHYSICAL ORIGIN OF MULTI-WAVELENGTH EMISSION

3.1. Particle transport and radiative processes

We model the spectral evolution of the jet by solving the time-dependent, coupled transport equations. In this work, we mainly solve Equation 1 and 2 using the AGN module of AMES (e.g., K. Murase 2022; B. T. Zhang & K. Murase 2023; A. Das et al. 2024).

$$\begin{aligned} \frac{\partial n_{\varepsilon_e}^e}{\partial t} = & -\frac{n_{\varepsilon_e}^e}{t_{\text{esc}}^e} - \frac{\partial}{\partial \varepsilon_e} \left[(P_{\text{syn}}^e + P_{\text{IC}}^e) n_{\varepsilon_e}^e \right] \\ & + \frac{\partial}{\partial t} \left(n_{\varepsilon_e}^{\gamma\gamma} + n_{\varepsilon_e}^{\text{BH}} + n_{\varepsilon_e}^{\text{phmes}} + n_{\varepsilon_e}^{\beta\text{-dec}} \right) + \dot{n}_{\varepsilon_e}^{\text{inj}}. \end{aligned} \quad (1)$$

$$\begin{aligned} \frac{\partial n_{\varepsilon_\gamma}^\gamma}{\partial t} = & -n_{\varepsilon_\gamma}^\gamma \left(\frac{1}{t_{\text{esc}}^\gamma} + \frac{1}{t_{\gamma\gamma}} \right) \\ & + \frac{\partial}{\partial t} \left(n_{\varepsilon_\gamma}^{\text{syn}} + n_{\varepsilon_\gamma}^{\text{IC}} + n_{\varepsilon_\gamma}^{\text{phmes}} \right) + \dot{n}_{\varepsilon_\gamma}^{\text{inj}}. \end{aligned} \quad (2)$$

The time evolution of the electron energy distribution $n_{\varepsilon_e}^e$ is described by the transport equation that includes particle escape, energy losses, secondary particle injection, and primary electron injection. The first term on the right-hand side accounts for electron escape with a characteristic timescale t_{esc}^e . The second term describes energy losses due to synchrotron radiation and IC scattering, with loss rates P_{syn}^e , P_{IC}^e , respectively. The third term represents the injection of secondary electrons and positron pairs produced via $\gamma\gamma$ pair production, Bethe-Heitler pair production, photomeson production interactions, and neutron β -decay. Finally, $\dot{n}_{\varepsilon_e}^{\text{inj}}$ denotes the primary electron injection rate. The time evolution of the photon number density $n_{\varepsilon_\gamma}^\gamma$ is governed by the transport equation. The loss terms include photon escape from

¹⁰ <https://icecube.github.io/skylh/master/html/index.html>

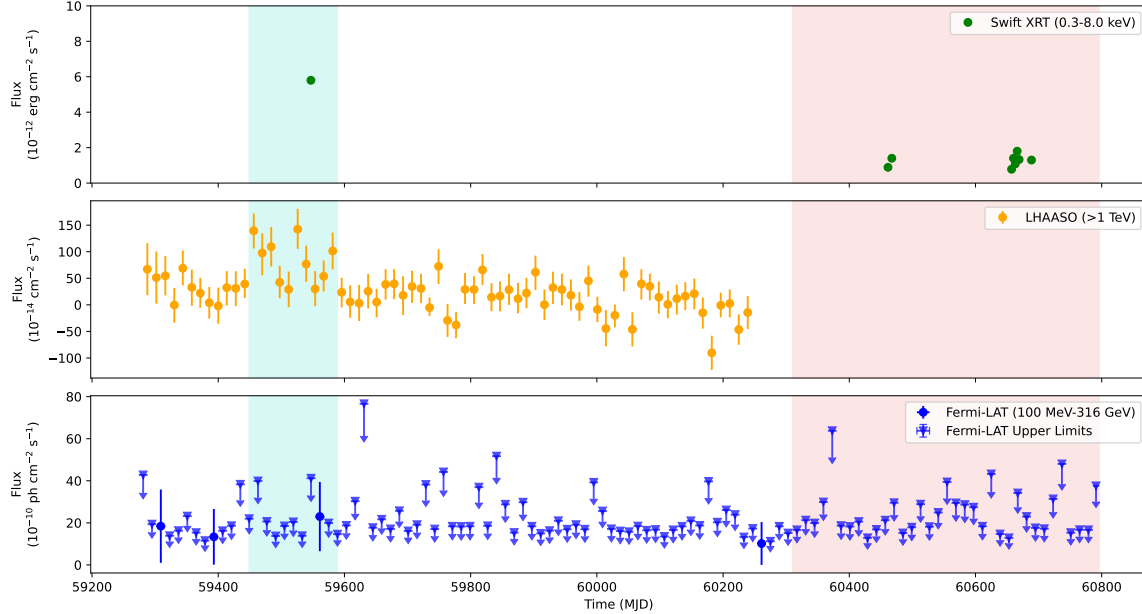


Figure 1. Multiwavelength light curve. We mainly focus on two time periods. The first period (cyan band) corresponds to the LHAASO flaring state, from MJD 59449 to MJD 59589 (Z. Cao et al. 2024b). The second period (pink band) spans from MJD 60310 to MJD 60796. For the Swift-XRT data, we show the flux per observation. For the Fermi-LAT light curve, we use a time binning of 7 days.

Table 1. Results of the analysis NGC 4278 neutrino flux by IceCube’s 10 year public data.

Method	n_s	γ	TS	$-\log_{10}(p_{\text{local}})$	$\Phi_0 @ 1 \text{ TeV} (\text{TeV}^{-1} \text{s}^{-1} \text{cm}^{-2})$
Time integration	11	3.6	0.83	0.48	3.7×10^{-13} (90% Sensitivity)
Time dependent	2.0	1.9	8.2	0.69	8.0×10^{-13} (90% Upper Limit)

the emission region and absorption via $\gamma\gamma$ interactions, while the source terms arise from synchrotron emission, IC scattering, photohadronic-induced cascades, and primary photon injection.

The acceleration process is parametrized by a characteristic timescale $t_{\text{acc}} \approx \eta \frac{\varepsilon'}{eB'c}$, where ε' is the particle energy in the comoving frame, B' is the magnetic field strength, and $\eta \geq 1$ is a factor characterizing the acceleration efficiency (with $\eta = 1$ corresponding to the Bohm limit) (L. Sironi et al. 2015). For photons, the escape timescale is the light-crossing time of the emission region, $t_{\text{esc},\gamma} = R'/c$. For charged particles, we assume an escape timescale of $t_{\text{esc}} = R'/c$.

The escape of charged particles from the blob is often described by the diffusive processes, with $t_{\text{esc}} \approx R'^2/2D$, where D is the diffusion coefficient. Here, we consider the advective escape, which can be approximated as $t_{\text{esc}} \approx R'/c$. This kind of advection escape is dominant when the magnetic field is significantly amplified at

the blob by some mechanism, and such a amplified field quickly decays with a dynamical timescale of R'/c . The adiabatic cooling is neglected, considering we consider a cylindrical geometry and the non-expanding blob.

We assume the primary electrons and protons are injected with a power-law spectrum featuring an exponential cutoff:

$$\dot{n}_{\varepsilon_e}^{\text{inj}} \propto \varepsilon_e'^{-s} \exp\left(-\frac{\varepsilon_e'}{\varepsilon_e'^{\text{max}}}\right), \quad (3)$$

where s is the spectral index and $\varepsilon_e'^{\text{max}}$ is the maximum cutoff energy.

For leptonic radiative processes, we consider synchrotron emission, IC scattering, and two-photon pair production. The synchrotron cooling timescale is given by:

$$t_{\text{syn}} = \frac{p}{|p|_{\text{syn}}} \approx \frac{3m^4 c^3}{4\sigma_T m_e^2 c^2} \frac{1}{\gamma \beta^2 U_B'}, \quad (4)$$

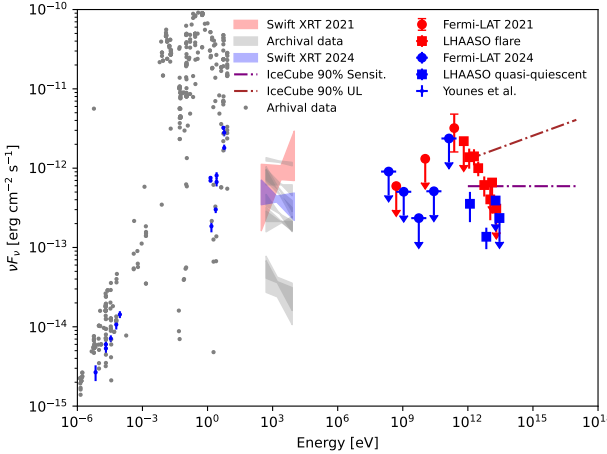


Figure 2. Broadband SED of NGC 4278. The archival data (small blue points) (G. Younes et al. 2010) correspond to radio and optical observations. The other archival data (small gray points) is obtained from SSDC^a. The archival X-ray spectrum (gray band) is obtained from Chandra and XMM-Newton observations (S. Pellegrini et al. 2012), where the upper band corresponds to the XMM-Newton observation in 2004 and the lower band to the Chandra observation in 2007. The X-ray spectrum (pink band) (J.-S. Lian et al. 2024) is from Swift–XRT observations in 2021, while the quasi-quiescent X-ray state (blue band) is from Swift–XRT observations in 2024. The GeV data point (red square) (E. Bronzini et al. 2024) is from Fermi–LAT observations in 2021, and the blue square represent our result which by analyzing Fermi–LAT data from 2024. The VHE data (red and blue dot) (Z. Cao et al. 2024b) are obtained from LHAASO observations during an active phase of this source. The brown dash-dotted line is the neutrino 90% sensitivity of IceCube with a spectral index of 2.0 (M. G. Aartsen et al. 2020). The purple dash-dotted line is the neutrino 90% upper limit from this work.

^a<https://tools.ssdc.asi.it/SED/>

where $U'_B = B'^2/8\pi$ is the magnetic energy density, σ_T is the Thomson cross-section.

The IC cooling timescale for relativistic electrons is expressed as:

$$t_{\text{IC}} \approx \frac{3m_e c}{4\sigma_T U'_{\text{ph}} \gamma F_{\text{KN}}}, \quad (5)$$

where U'_{ph} is the target photon field energy density and F_{KN} is the Klein-Nishina correction factor (G. R. BLUMENTHAL & R. J. GOULD 1970).

The optical depth for two-photon annihilation ($\gamma\gamma \rightarrow e^+e^-$) is calculated as:

$$\tau_{\gamma\gamma}(\varepsilon'_\gamma) = \frac{R'}{c} \int d\Omega \int d\varepsilon_* n_{\text{ph}}(\varepsilon_*, \Omega) \sigma_{\gamma\gamma}(\varepsilon'_\gamma, \varepsilon_*, \mu) (1-\mu)c, \quad (6)$$

where ε_* is the target photon energy, $\mu = \cos\theta$ is the interaction angle, and $\sigma_{\gamma\gamma}$ is the pair-production cross-section.

3.2. Fitting Method

We employ the MCMC software `emcee` (v3.1.6) (D. Foreman-Mackey et al. 2013) to fit the broadband SED of NGC 4278 using AMES. The best-fit parameters are listed in Table 2.

The log-likelihood function ($\ln \mathcal{L}$) incorporates both detected data points and upper limits (UL). We model the uncertainties of detected points as Gaussian, adopting a 10% fractional error for the IR and optical datasets. For upper limits, we calculate the probability that the true flux lies below the limit (left-censored data) using the Gaussian Cumulative Distribution Function (CDF), $\Phi(z)$. We assign a conservative systematic uncertainty of 10% ($\sigma_i = 0.1y_{\text{UL}}$) to the upper limits. The total log-likelihood is defined as:

$$\ln \mathcal{L}_{\text{total}} = \sum_i \begin{cases} -\frac{1}{2} \left[\frac{(y_i - \mu_i)^2}{\sigma_i^2} + \ln(2\pi\sigma_i^2) \right] & \text{for detections} \\ \ln \Phi \left(\frac{y_i - \mu_i}{\sigma_i} \right) & \text{for UL} \end{cases}, \quad (7)$$

where y_i is the observed flux (or UL value), μ_i is the model-predicted flux, and σ_i is the flux error (or assigned UL uncertainty).

4. RESULTS

4.1. One-zone SSC model

4.1.1. Quasi-quiescent state

The SED in the quasi-quiescent state is well-reproduced by a one-zone leptonic SSC model, as shown in Figure 3. The shaded band represents the 1σ uncertainty region derived from the MCMC fitting. The contour plot is shown in the left panel in Figure 7. The injected electron energy distribution is characterized by a spectral index of $s_e \simeq 2.4$, with minimum and maximum Lorentz factors of $\gamma'_{\text{min}} \simeq 1.0 \times 10^3$ and $\gamma'_{\text{max}} \simeq 9.9 \times 10^6$, respectively. The magnetic field strength in the comoving frame is $B' \simeq 0.4$ mG. The derived electron spectrum is noticeably softer than that inferred for the flaring state discussed later (see also J.-S. Lian et al. (2024); S. Dutta & N. Gupta (2024); Z.-R. Wang et al. (2024)). We estimate the observed synchrotron peak energy as:

$$\varepsilon_{\text{syn,pk}} \approx (1+z) \delta \frac{\gamma_e^2 \hbar e B'}{m_e c} \simeq 1.2 \times 10^3 \left(\frac{B'}{0.4 \text{ mG}} \right) \left(\frac{\gamma_e}{10^7} \right)^2 \text{ eV}, \quad (8)$$

consistent with the modeled synchrotron peak shown in Figure 3.

The corresponding total jet power in the black hole rest frame is estimated as (K. Murase et al. 2012).

$$P_{\text{jet}} = 2\pi R'^2 \beta c \Gamma^2 (u'_B + u'_e) \simeq 8.0 \times 10^{42} \text{ erg s}^{-1}, \quad (9)$$

which is approximately four times higher than the jet power inferred from radio observations (G. Giovannini et al. 2004).

Table 2. Physical parameters derived from SSC modeling. Median values and 1σ confidence intervals for the SED model parameters of NGC 4278 during quasi-quiescent and flaring states.

Parameter	Quasi-quiescent (2024–2025)	Flare (2021)
B' [mG]	$0.40^{+0.40}_{-0.10}$	$29.80^{+137.80}_{-26.30}$
R' [cm]	$7.31^{+2.46}_{-4.86} \times 10^{17}$	$2.03^{+2.09}_{-1.68} \times 10^{15}$
s_e	$2.43^{+0.03}_{-0.03}$	$1.88^{+0.26}_{-0.24}$
$\gamma'_{e,\text{min}}$	$1.01^{+0.28}_{-0.72} \times 10^3$	$1.05^{+2.67}_{-0.83} \times 10^3$
$\gamma'_{e,\text{max}}$	$9.94^{+2.87}_{-3.11} \times 10^6$	$1.87^{+2.85}_{-1.07} \times 10^7$
L'_e [erg s $^{-1}$]	$3.92^{+1.19}_{-1.90} \times 10^{42}$	$1.45^{+4.92}_{-0.70} \times 10^{41}$

As mentioned in the previous section, we initially fixed the Doppler factor at $\delta = 2.7$ when fitting the multi-wavelength data. However, under this assumption, the predicted VHE γ -ray flux in the quasi-quiescent state is lower than the LHAASO measurements by a factor of ~ 2 . We therefore treated δ as a free parameter, and the resulting best-fit spectrum, shown in Figure 3, provides a satisfactory description of the LHAASO observations, see the contour plots in the Appendix. For the best-fit model, the total jet power is estimated to be $P_{\text{jet}} \simeq 1.1 \times 10^{42}$ erg s $^{-1}$ with $\delta \simeq 6.3$, consistent with radio observations. The best-fit radius $R' \sim 10^{14.97}$ cm indicates a compact emission region, where a larger Doppler factor may be justified by the higher bulk Lorentz factors expected in the inner jet near the SMBH (B. G. Piner & P. G. Edwards 2004). Furthermore, Figure 8 presents the best-fit spectrum obtained by varying δ in the range of 1–12 using the marginalized maximum-likelihood method. We find a preferred value of $\delta \sim 6$, which is consistent with the SED fitting results shown in Figure 3.

We also evaluate the VHE gamma-ray origin within the context of external inverse-Compton (EIC) and lepto-hadronic scenarios in the following sections.

4.1.2. Flaring State

The SED fitting for the flaring state, using a one-zone leptonic SSC model, is represented by the red line in Figure 3. This fit incorporates X-ray, γ -ray, and

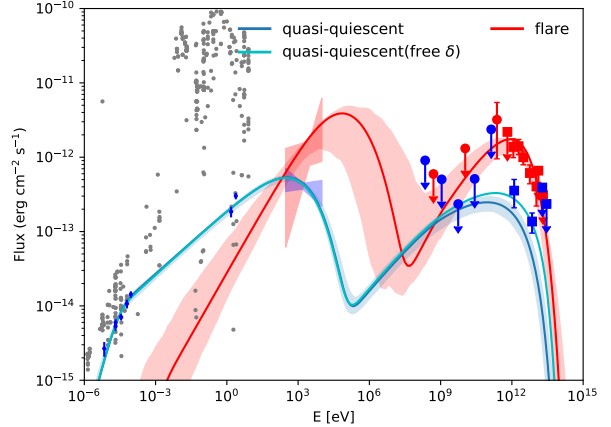


Figure 3. The broadband SED modeled with one-zone SSC model. The solid red and blue lines represent the SED computed using the 50th percentile (median) of the parameter distributions for the flaring and quasi-quiescent states, respectively. The surrounding red and blue bands indicate the 1σ uncertainty of the fitting parameters.

LHAASO data. Following the approach used for the quasi-quiescent state, the Doppler factor was fixed at $\delta = 2.7$. The fitted blob radius is $R' \simeq 2.0 \times 10^{15}$ cm. This comoving size can be independently estimated from the observed variability as $R' \approx \delta c t_{\text{var}} / (1 + z) \simeq 4.1 \times 10^{17}$ cm, adopting $t_{\text{var}} = 58$ days (Z. Cao et al. 2024b). Our fitted value for R' is significantly smaller than this variability-derived upper limit, implying a more compact emission region. The magnetic field strength was found to be $B' \simeq 29.8$ mG. For the electron distribution, we obtained a spectral index $s_e \simeq 1.9$, Lorentz factors $\gamma'_{\text{min}} \simeq 1.1 \times 10^3$ and $\gamma'_{\text{max}} \simeq 1.9 \times 10^7$, and a luminosity $L'_e \simeq 1.5 \times 10^{41}$ erg s $^{-1}$. These parameters are summarized in Table 2. The total power of the two-sided jet is $P_{\text{jet}} \simeq 2.5 \times 10^{41}$ erg s $^{-1}$, which is lower than the jet kinetic energy derived from radio measurements (G. Giovannini et al. 2004). We estimate the synchrotron peak energy as: $E_{\text{syn,pk}} \simeq 3.1 \times 10^5$ eV. However, due to the lack of hard X-ray data, the synchrotron peak energy remains difficult to constrain precisely. Our fitting results are generally consistent with those of J.-S. Lian et al. (2024) and S. Dutta & N. Gupta (2024), though our derived emission region radius is smaller by a factor of approximately five. In their study, J.-S. Lian et al. (2024) modeled the SED using a broken power-law electron distribution and an assumed radius of $R' = 1 \times 10^{16}$ cm. While they also fixed $\delta = 2.7$ based on VLBA observations (G. Giovannini et al. 2004), they explored an alternative scenario with $\delta = 10$ based on TeV BL Lac studies (F. Tavecchio et al. 2010; J. Zhang et al. 2012). The discrepancies between our results and those of J.-S.

Lian et al. (2024) likely stem from the use of different Fermi-LAT datasets; specifically, we adopt the results from E. Bronzini et al. (2024), which provide a more stringent upper limit.

4.2. EIC Model

In this section, we evaluate the contribution of external photon fields—specifically from the accretion disk—to the production of high-energy emission. While the SSC model considers internal synchrotron photons, the upscattering of external photons in EIC model can also significantly contribute to the VHE gamma-ray flux. It has been widely discussed that the observed X-ray emission from LL AGN comes from the hot accretion disk. Radiatively inefficient accretion flows (RIAFs) in LL AGN could produce multi-wavelength emission across X-ray band by thermal electrons (Das et. al., in preparation), and we utilize the one-zone model provided by (S. S. Kimura & K. Toma 2020; S. S. Kimura et al. 2021a,b). In the comoving frame of the blob, the target photon density from the inner disk is de-boosted by the relativistic motion of the jet. The comoving photon energy density can be estimated as:

$$\varepsilon'^2 \frac{dn}{d\varepsilon'} = \delta_{D,\text{de}}^4 \frac{d_L^2 E F_E}{l^2 c}, \quad (10)$$

where l represents the distance from the SMBH to the emission blob measured in SMBH frame, $\delta_{D,\text{de}} = 1/\Gamma(1+\beta)$, $\varepsilon' = \delta_{D,\text{de}} E(1+z)$. We estimate the distance of $l \approx R'/\delta_D \theta_j$, where $\delta_D = 1/\Gamma(1-\beta)$ is the Doppler factor. The jet velocity $\beta = 0.76$ and the half-opening angle is $\theta_j = 20^\circ$. Although the photon field from the accretion disk is inherently anisotropic, we assume an isotropic distribution in our calculations, under the assumption that the high-energy electrons are isotropically distributed in the comoving frame. The discrepancy introduced by neglecting the full anisotropic IC scattering cross section is expected to be approximately a factor of two (B. T. Zhang & K. Murase 2023).

Our results are shown in Figure 4. The dashed curves are the SED from our RIAF model (S. S. Kimura & K. Toma 2020; S. S. Kimura et al. 2021a,b), in both flaring and quasi-quiescent states, where the difference mainly due to accretion rate. The accretion rate in quasi-quiescent state is $\dot{m} = 6 \times 10^{-4}$, while it is $\dot{m} = 10^{-3}$ in the flaring state. The other parameters are keep the same, with the alpha parameter $\alpha = 0.4$ and plasma beta parameter $\beta = 0.7$. The best-fit parameters are summarized in Table 3. In the EIC scenario, a harder spectral index of electrons is injected to explain VHE gamma-rays, while the X-ray is fully explained with the RIAF model. Compare the SSC

Table 3. Similar to Table 2, physical parameters used in EIC modeling.

Parameter	quasi-quiescent	flare
Γ	1.5	1.5
θ°	20	20
B' [mG]	100	16
R' [cm]	2.63×10^{15}	1.74×10^{16}
s_e	1.50	1.58
γ'_e,min	8.91×10^2	9.12×10^2
γ'_e,max	4.17×10^7	1.86×10^7
L'_e [erg s $^{-1}$]	1.78×10^{39}	1.10×10^{40}

model, the EIC model provides a more reasonable explanation of the production of VHE gamma-rays in the quasi-quiescent state for the fixed value of Doppler factor $\delta = 2.7$. The corresponding total jet power is estimated as $P_{\text{jet}} \simeq 1.3 \times 10^{39}$ erg s $^{-1}$ (quasi-quiescent) and $P_{\text{jet}} \simeq 9.5 \times 10^{39}$ erg s $^{-1}$ (flare), which are smaller than the total jet power inferred from radio observations. We estimate the blob positions to be $l \sim 5 \times 10^{15}$ cm and 3.3×10^{16} cm for the quasi-quiescent and flaring states, respectively. Both values are compact compared to the radio emission region of the jet.

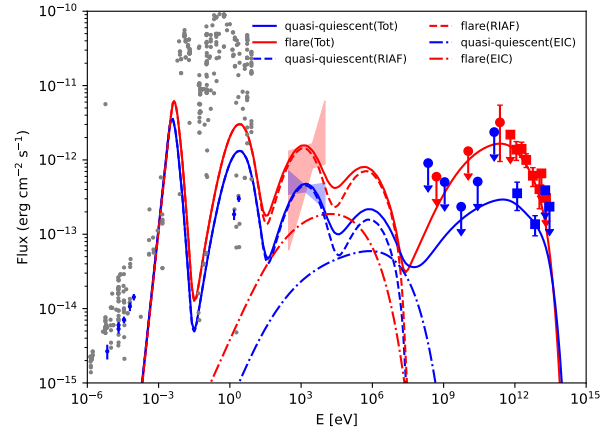


Figure 4. Multi-wavelength emission predicted by the EIC model. The solid curves represent the total emission, while the dashed and dash-dotted curves denote the contributions from the RIAF and EIC components, respectively.

4.3. Lepto hadronic model

In addition to pure leptonic processes, VHE gamma rays can be also produced from protons, including proton synchrotron emission, decay of neutral pions, and associated cascade emission from the pp and $p\gamma$ processes (e.g., S. Dimitrakoudis et al. 2012; M. Böttcher et al. 2013; S. Gao et al. 2017; A. Keivani et al. 2018;

K. Murase 2022). Nevertheless, in this study, we adopt the best-fit leptonic results as the baseline parameters for our lepto hadronic calculations, rather than scanning the entire parameter space for lepto hadronic modeling as in the previous section. This means that entire photon spectra is described by the leptonic process, but we introduce some amount of protons to evaluate the neutrino production in this system.

Similar to the electrons, the injected protons are assumed to follow a power-law energy distribution with an exponential cutoff, characterized by a fixed spectral index of $s_p = 2$. The maximum proton energy is determined by balancing the acceleration timescale with the diffusive timescale in the Bohm limit, yielding a maximum Lorentz factor of $\gamma'_{p,\max} m_p c^2 \sim \eta^{-1} eB'R'$, where $\eta = 10$ is a numerical factor. The estimated value of $\gamma'_{p,\max}$ are 9.9×10^6 (SSC, quasi-quiescent), 1.9×10^6 (SSC, flare), 8.6×10^6 (EIC, quasi-quiescent) and 8.9×10^6 (EIC, flare). The minimum proton energy is $\varepsilon'_{p,\min} = 10^9$ eV. The injected proton luminosity is fixed at $L'_p = 3.9 \times 10^{43}$ erg s $^{-1}$, roughly 0.1% of the Eddington luminosity, which is consistent with the energy budget estimated by RIAF modeling in EIC scenario. The observed jet power of NGC 4278 is estimated to be only $\sim 10^{42}$ erg s $^{-1}$, but we adopted the value above based on our RIAF modeling. Our choice of jet power is rather conservative, comparing the neutrino emission modeling in blazars (e.g., K. Murase et al. 2014; M. Petropoulou et al. 2015), where the jet power close to the Eddington luminosity is often adopted.

We include photomeson production, photopair production, and proton-proton (pp) interaction processes in the calculation. The number density of cold protons in the comoving frame is assumed to be equal to that of the electrons, $n'_{p,\text{cold}} = n'_e \simeq L'_e / (4\pi R'^2 c \gamma'_{e,\min} m_e c^2)$, and these protons serve as the targets for pp interactions. The detailed SEDs are presented in Figure 5. The cascade emissions from photomeson production and Bethe-Heitler pair production are shown separately; both lie well below the observed SED.

The results of the all-flavor neutrino spectrum are summarized in Figure 6. Given the IceCube effective area, we calculated the expected number of neutrinos for a time window $T = 58$ days for the flaring state and $T = 15$ yr for the quasi-quiescent state, respectively. The number of muon neutrinos (and antineutrinos) can be estimated as

$$\mathcal{N}_{\nu_\mu} = T \times \int_{E_{\text{th}}}^{\infty} dE \phi_\nu(E) \times A_{\text{eff}}(E, \text{Dec.}), \quad (11)$$

where A_{eff} is the IceCube effective area at Dec. = 29.281° (M. Aartsen et al. 2018), $E_{\text{th}} = 50$ TeV is the energy threshold, ϕ_ν is the modeled neutrino flux.

The expected detection number are $\mathcal{N}_{\nu_\mu} = 1.2 \times 10^{-3}$ (EIC, quasi-quiescent), $\mathcal{N}_{\nu_\mu} = 3.6 \times 10^{-4}$ (SSC, quasi-quiescent), $\mathcal{N}_{\nu_\mu} = 4.0 \times 10^{-5}$ (SSC, flare), $\mathcal{N}_{\nu_\mu} = 7.1 \times 10^{-6}$ (EIC, flare). Thus, it is possible for IceCube to detect high-energy neutrinos from NGC 4278 based on our model in the promising case, especially in the EIC model in the quasi-quiescent state.

5. DISCUSSION AND SUMMARY

In this study, we conducted a long-term multi-wavelength analysis of the radio galaxy NGC 4278 during the 2024–2025 period, identifying the jet in a quasi-quiescent state. We performed numerical modeling of this state and compared it with the 2021 flaring state. Using a one-zone leptonic SSC model combined with MCMC analysis, we derived best-fit parameters and 1σ uncertainty bands for both epochs. While the origin of the VHE gamma-ray emission in the flaring state is consistent with the SSC model, the model fails to explain the VHE gamma-rays in the quasi-quiescent state. Specifically, the SSC model requires a jet power that significantly overshoots observed values, unless a Doppler factor higher than that measured from radio observations is adopted.

A plausible explanation for the discrepancy between the model predictions and the observations is the use of non-simultaneous multi-wavelength data in constructing the SED for the quasi-quiescent state. For instance, the average flux of VHE γ -rays observed in 2024–2025 corresponds to a relatively low state. Alternatively, the VHE γ -rays detected by LHAASO during the quasi-quiescent state may receive contributions from other emission regions. For example, the VHE γ -rays from NGC 4278 could originate from hadronic interactions between cosmic-ray protons and ions that have escaped from the jet and subsequently interacted with surrounding giant molecular clouds (A. Shoji et al. 2025; J.-L. Xu et al. 2025). However, reproducing the LHAASO-observed flux in this scenario requires an enhanced accretion rate by a factor of ~ 10 –1000, and a diffusion coefficient that is 0.1–1 times lower than that inferred for the general interstellar medium.

In LL AGNs, X-ray emission may be associated with the accretion flow (A. Das et al. 2026). The infrared component from RIAFs can also serve as a target photon field for the EIC process, which successfully explains the observed VHE gamma-rays using physically reasonable values for both the Doppler factor and jet power. Our results suggest that the EIC process may play a critical role in the production of VHE gamma-rays in LL AGNs.

Finally, we explored a lepto hadronic model, comparing the predicted neutrino flux to the observational up-

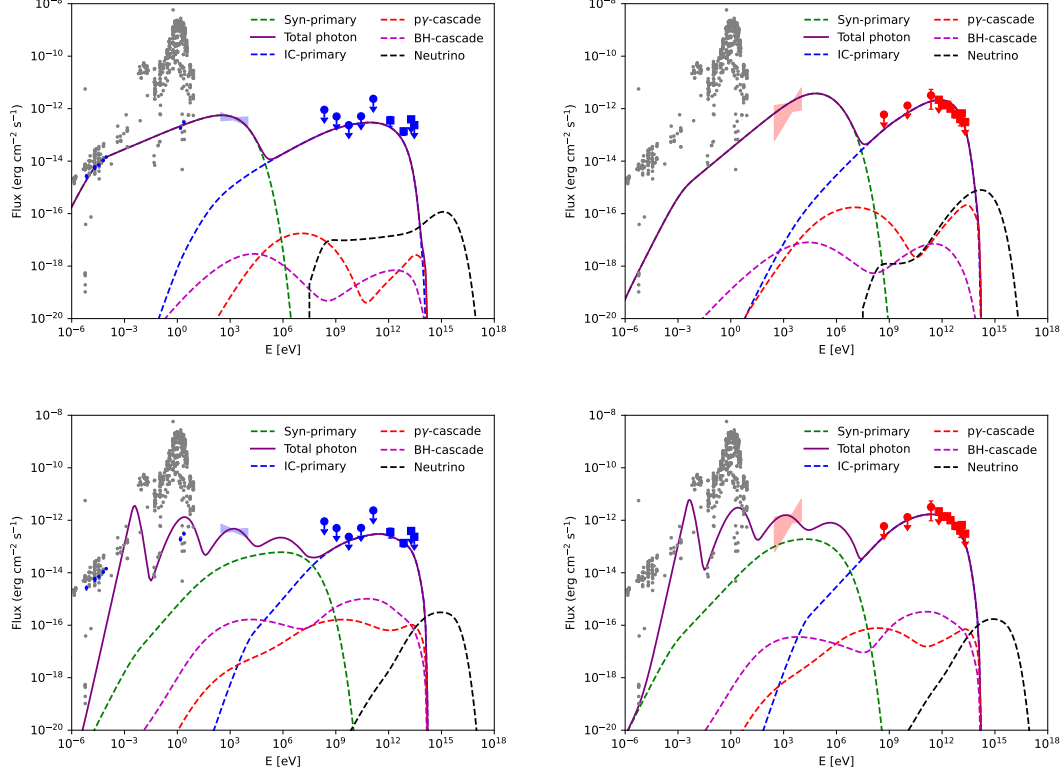


Figure 5. Leptohadronic model from the injection of high-energy protons. The black dashed lines show the all-flavor neutrino spectrum, while the green, blue, red, and purple dashed lines represent the synchrotron emission from primary electrons, IC emission from primary electrons, cascade emission from the photomeson production process, and cascade emission from the Bethe-Heitler pair production process, respectively. Top left: quasi-quiescent state (SSC); Top right: flaring state (SSC); Bottom left: quasi-quiescent state (EIC); Bottom right: flaring state (EIC).

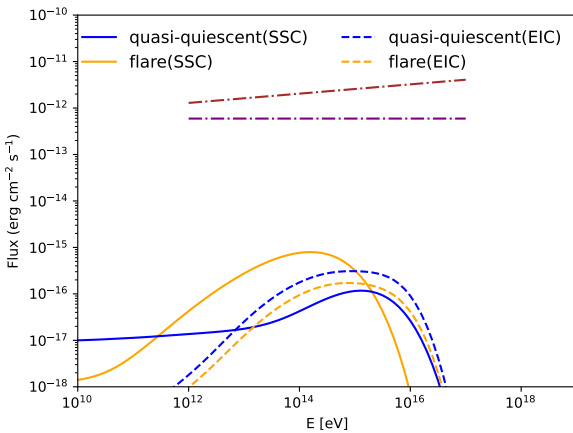


Figure 6. Predicted all-flavor neutrino spectra for the SSC and EIC scenarios in quasi-quiescent and flaring states. Red and purple dash-dotted lines denote the 90% upper limit (time-dependent search) and 90% sensitivity (time-integrated search) from Table 1.

per limits derived in this work. Our results showed that the detection of high-energy neutrinos from NGC 4278 is

possible assuming roughly 0.1% of the Eddington luminosity transferred to high-energy protons. Future multi-messenger observations of LL AGNs will be essential to further constrain the physical processes responsible for the production of high-energy gamma-rays and neutrinos.

ACKNOWLEDGMENTS

We gratefully acknowledge the valuable discussions and insightful comments provided by Shiqi Yu, Feng Qi and Alberto Dominguez. B.T.Z. is supported in China by National Key R&D program of China under the grant 2024YFA1611402. The work of K.M. was supported by the NSF Grant No. 2308021. S.S.K. acknowledges support by KAKENHI Nos. 22K14028, 21H04487, 23H04899, and the Tohoku Initiative for Fostering Global Researchers for Interdisciplinary Sciences (TI-FRIS) of MEXT’s Strategic Professional Development Program for Young Researchers.

APPENDIX

A. DETAILS OF DATA ANALYSIS RESULT

We analyzed the Swift-XRT data for NGC 4278. Table 5 lists all the Swift-XRT observations used in this work. The table includes the observation date, observation ID (ObsID), exposure time, and the best-fit model parameters. Additionally, we combined the observational data from 2024 to 2025 to perform the SED fitting. These combined results are also presented in the table 4. In fitting model, for the Galactic hydrogen column density, we fixed it to be $2.2 \times 10^{20} \text{ cm}^{-2}$ (R. Willingale et al. 2013), and we performed a fit to the excess hydrogen column density, photon index, and flux with C-statistic by XSPEC. We performed an analysis of the multiwavelength light curve 1. The results show a simultaneous high state in 2021, with elevated flux in both the X-ray and LHAASO energy range.

Table 4. Best-fit parameters for the Swift-XRT spectrum (2024–2025). Uncertainties correspond to the 90% confidence level.

Galactic N_{H}	0.022 (fixed)	10^{22} cm^{-2}
Excess N_{H}	$0.058^{+0.039}_{-0.035}$	10^{22} cm^{-2}
Redshift (z)	0.00216	–
Photon Index (Γ)	$2.11^{+0.17}_{-0.16}$	–
Obs Flux (F_{obs})	$1.17^{+0.11}_{-0.10}$	$10^{-12} \text{ erg cm}^{-2} \text{ s}^{-1}$
Unabs Flux (F_{unabs})	$1.43^{+0.14}_{-0.11}$	$10^{-12} \text{ erg cm}^{-2} \text{ s}^{-1}$
C-stat / DOF	252.9/283	–
Goodness (χ^2)	268.0	–
Net Count Rate	0.027	counts s^{-1}
Exposure Time	26.8	ksec

Table 5. Log of Swift-XRT observations of NGC 4278 and spectral fitting results. Fluxes are in the 0.3–10.0 keV band. The Galactic column density was fixed at $N_{\text{H}} = 2.22 \times 10^{20} \text{ cm}^{-2}$. Errors correspond to the 90% confidence level.

Date(UT)	ObsID	Exposure (s)	Γ	N_{H} (Intrinsic) (10^{20} cm^{-2})	Flux(0.3–10.0 keV) ($10^{-12} \text{ erg/cm}^2/\text{s}$)
2021-02-26 11:13:35	03109562001	173.0	–	–	–
2021-11-28 20:16:34	03109562002	922.7	$1.2^{+0.7}_{-0.3}$	$0^{+17.9}_{-0}$	$4.5^{+1.6}_{-1.7}$
2024-05-31 07:47:56	00016648001	1662.3	$2.3^{+0.7}_{-0.4}$	$0^{+0.12}_{-0}$	$0.89^{+0.3}_{-0.25}$
2024-06-03 05:21:54	00016648002	1632.3	–	–	–
2024-06-06 09:03:56	00016648003	1559.5	$1.9^{+0.7}_{-0.5}$	$6.2^{+19.4}_{-6.2}$	$1.4^{+0.7}_{-0.4}$
2024-12-13 03:54:29	00016648004	3638.1	$2.0^{+0.6}_{-0.3}$	$0.19^{+11.82}_{-0.19}$	$0.78^{+0.19}_{-0.21}$
2024-12-16 03:56:57	00016648005	2033.4	$1.9^{+0.6}_{-0.5}$	11^{+20}_{-11}	$1.4^{+0.6}_{-0.4}$
2024-12-19 01:02:56	00016648006	4360.2	$2.2^{+0.4}_{-0.3}$	3^{+9}_{-3}	$1.08^{+0.25}_{-0.21}$
2024-12-22 01:10:57	00016648007	4327.6	$1.79^{+0.36}_{-0.39}$	$3.8^{+10.1}_{-3.8}$	$1.8^{+0.4}_{-0.3}$
2024-12-25 03:10:57	00016648008	4415.4	$2.1^{+0.4}_{-0.3}$	4^{+9}_{-4}	$1.33^{+0.32}_{-0.25}$
2024-12-06 22:50:25	00089850001	1575.8	–	–	–
2025-01-13 17:12:55	00089850002	1582.1	$2.4^{+0.9}_{-0.8}$	$0.17^{+0.27}_{-0.17}$	$1.3^{+0.7}_{-0.4}$

B. FITTING RESULTS OF SSC MODEL

Here, we present the contour plots of the fitting results in the one-zone SSC model in Figure 7. In Figure 8, we present the fitting results with the Doppler factor as a free parameter in both marginalized maximum-likelihood method (left panel) and MCMC fitting (right panel).

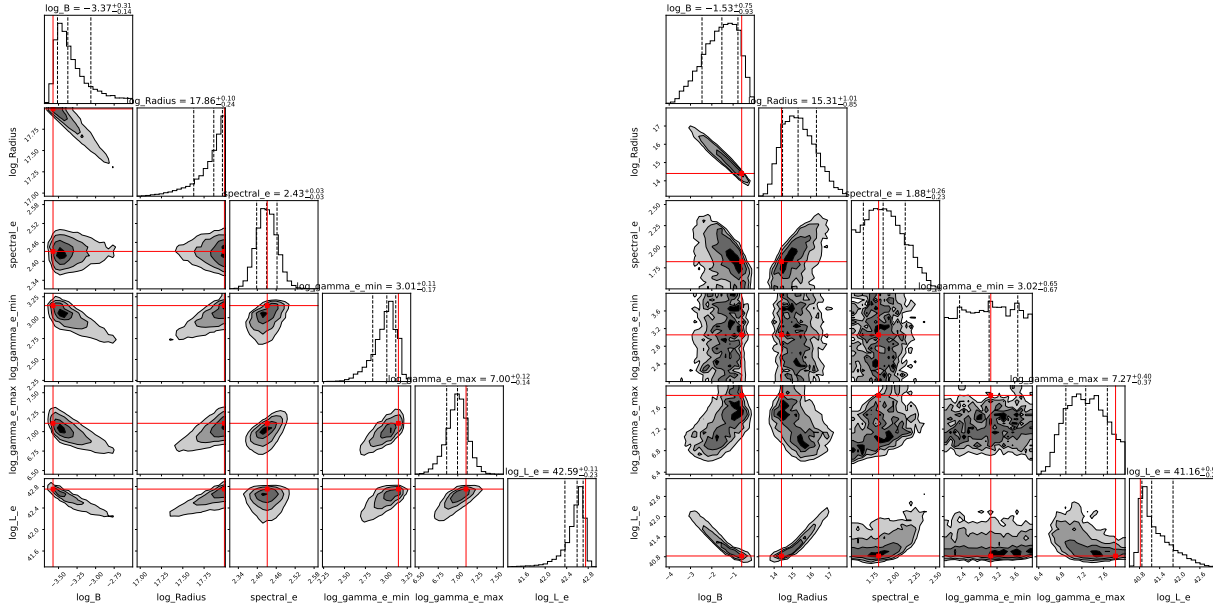


Figure 7. Contour plot in the quasi-quiescent state (left panel) and flaring state (right panel) for fixed Doppler factor δ , respectively.

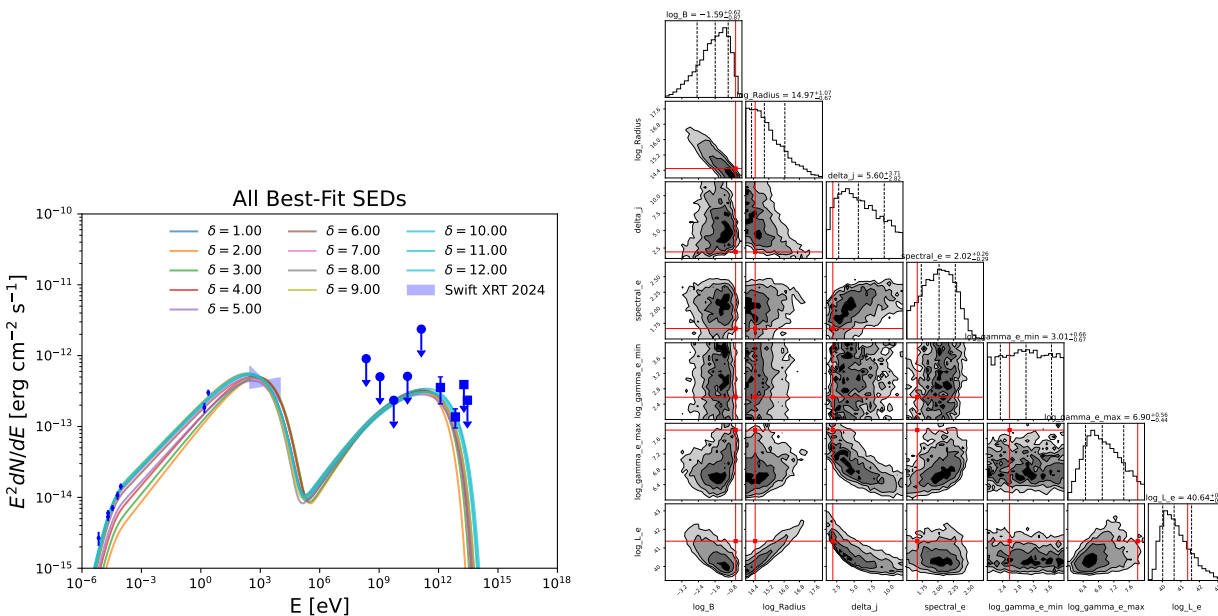


Figure 8. Left: The marginalized maximum-likelihood method with the variation of Doppler factor δ . Right: Contour plot in the quasi-quiescent state with δ as free parameter.

REFERENCES

Aartsen, M., Ackermann, M., Adams, J., et al. 2018, *Science*, 361, 147–151, doi: [10.1126/science.aat2890](https://doi.org/10.1126/science.aat2890)

Aartsen, M. G., et al. 2020, *Phys. Rev. Lett.*, 124, 051103, doi: [10.1103/PhysRevLett.124.051103](https://doi.org/10.1103/PhysRevLett.124.051103)

Abbasi, R., Ackermann, M., Adams, J., et al. 2021, PoS, ICRC2021, 1073, doi: [10.22323/1.395.1073](https://doi.org/10.22323/1.395.1073)

Abbasi, R., Ackermann, M., Adams, J., et al. 2022, *Science*, 378, 538–543, doi: [10.1126/science.abg3395](https://doi.org/10.1126/science.abg3395)

Abdollahi, S., Acero, F., Baldini, L., et al. 2022, *The Astrophysical Journal Supplement Series*, 260, 53, doi: [10.3847/1538-4365/ac6751](https://doi.org/10.3847/1538-4365/ac6751)

Ballet, J., Bruel, P., Burnett, T. H., Lott, B., & collaboration, T. F.-L. 2024, Fermi Large Area Telescope Fourth Source Catalog Data Release 4 (4FGL-DR4), <https://arxiv.org/abs/2307.12546>

Bellenghi, C., Karl, M., Wolf, M., et al. 2023, PoS, ICRC2023, 1061, doi: [10.22323/1.444.1061](https://doi.org/10.22323/1.444.1061)

BLUMENTHAL, G. R., & GOULD, R. J. 1970, *Rev. Mod. Phys.*, 42, 237, doi: [10.1103/RevModPhys.42.237](https://doi.org/10.1103/RevModPhys.42.237)

Böttcher, M., Reimer, A., Sweeney, K., & Prakash, A. 2013, *ApJ*, 768, 54, doi: [10.1088/0004-637X/768/1/54](https://doi.org/10.1088/0004-637X/768/1/54)

Braun, J., Dumm, J., De Palma, F., et al. 2008, *Astroparticle Physics*, 29, 299, doi: [10.1016/j.astropartphys.2008.02.007](https://doi.org/10.1016/j.astropartphys.2008.02.007)

Bronzini, E., Grandi, P., Torresi, E., & Buson, S. 2024, Fermi-LAT detection of the low-luminosity radio galaxy NGC 4278 during the LHAASO campaign, <https://arxiv.org/abs/2409.17255>

Cao, Z., et al. 2024a, *Astrophys. J. Suppl.*, 271, 25, doi: [10.3847/1538-4365/acfd29](https://doi.org/10.3847/1538-4365/acfd29)

Cao, Z., et al. 2024b, *Astrophys. J. Lett.*, 971, L45, doi: [10.3847/2041-8213/ad5e6d](https://doi.org/10.3847/2041-8213/ad5e6d)

Cavagnolo, K. W., McNamara, B. R., Nulsen, P. E. J., et al. 2010, *ApJ*, 720, 1066, doi: [10.1088/0004-637X/720/2/1066](https://doi.org/10.1088/0004-637X/720/2/1066)

Chiaberge, M., Capetti, A., & Macchetto, F. D. 2005, *ApJ*, 625, 716, doi: [10.1086/429612](https://doi.org/10.1086/429612)

Das, A., Zhang, B. T., & Murase, K. 2024, *Astrophys. J.*, 972, 44, doi: [10.3847/1538-4357/ad5a04](https://doi.org/10.3847/1538-4357/ad5a04)

Das, A., et al. 2026

Dimitrakoudis, S., Mastichiadis, A., Protheroe, R. J., & Reimer, A. 2012, *A&A*, 546, A120, doi: [10.1051/0004-6361/201219770](https://doi.org/10.1051/0004-6361/201219770)

Dutta, S., & Gupta, N. 2024, *The Astrophysical Journal*, 974, 56, doi: [10.3847/1538-4357/ad6d65](https://doi.org/10.3847/1538-4357/ad6d65)

Foreman-Mackey, D., Hogg, D. W., Lang, D., & Goodman, J. 2013, *Publications of the Astronomical Society of the Pacific*, 125, 306–312, doi: [10.1086/670067](https://doi.org/10.1086/670067)

Gao, S., Pohl, M., & Winter, W. 2017, *The Astrophysical Journal*, 843, 109, doi: [10.3847/1538-4357/aa7754](https://doi.org/10.3847/1538-4357/aa7754)

Garcia, A. M. 1993, *A&AS*, 100, 47

Giovannini, G., Giroletti, M., & Taylor, G. B. 2004, The two sided parsec scale structure of the Low Luminosity Active Galactic Nucleus in NGC 4278, <https://arxiv.org/abs/astro-ph/0412563>

González-Martín, O., Masegosa, J., Márquez, I., Guainazzi, M., & Jiménez-Bailón, E. 2009, *Astronomy & Astrophysics*, 506, 1107

Ho, L. C. 1999, *The Astrophysical Journal*, 516, 672

Ho, L. C. 2008, *Annu. Rev. Astron. Astrophys.*, 46, 475

IceCube Collaboration. 2021, IceCube Data for Neutrino Point-Source Searches Years 2008–2018, IceCube Neutrino Observatory, doi: [10.21234/CPKQ-K003](https://doi.org/10.21234/CPKQ-K003)

Keivani, A., et al. 2018, *Astrophys. J.*, 864, 84, doi: [10.3847/1538-4357/aad59a](https://doi.org/10.3847/1538-4357/aad59a)

Kimura, S. S., Kashiyama, K., & Hotokezaka, K. 2021a, *The Astrophysical Journal Letters*, 922, L15, doi: [10.3847/2041-8213/ac35dc](https://doi.org/10.3847/2041-8213/ac35dc)

Kimura, S. S., Murase, K., & Mészáros, P. 2021b, *Nature Communications*, 12, doi: [10.1038/s41467-021-25111-7](https://doi.org/10.1038/s41467-021-25111-7)

Kimura, S. S., & Toma, K. 2020, *The Astrophysical Journal*, 905, 178, doi: [10.3847/1538-4357/abc343](https://doi.org/10.3847/1538-4357/abc343)

Lian, J.-S., Li, J.-X., Hu, X.-K., et al. 2024, Origin of the Very High Energy γ -rays in the Low-luminosity Active Galactic Nucleus NGC 4278, <https://arxiv.org/abs/2405.00347>

Murase, K. 2022, *Astrophys. J. Lett.*, 941, L17, doi: [10.3847/2041-8213/aca53c](https://doi.org/10.3847/2041-8213/aca53c)

Murase, K., Dermer, C. D., Takami, H., & Migliori, G. 2012, *The Astrophysical Journal*, 749, 63, doi: [10.1088/0004-637x/749/1/63](https://doi.org/10.1088/0004-637x/749/1/63)

Murase, K., Inoue, Y., & Dermer, C. D. 2014, *Phys. Rev. D*, 90, 023007, doi: [10.1103/PhysRevD.90.023007](https://doi.org/10.1103/PhysRevD.90.023007)

Nagar, N. M., Falcke, H., & Wilson, A. S. 2005, *A&A*, 435, 521, doi: [10.1051/0004-6361:20042277](https://doi.org/10.1051/0004-6361:20042277)

Pellegrini, S., Wang, J., Fabbiano, G., et al. 2012, *The Astrophysical Journal*, 758, 94

Petropoulou, M., Dimitrakoudis, S., Padovani, P., Mastichiadis, A., & Resconi, E. 2015, *Mon. Not. Roy. Astron. Soc.*, 448, 2412, doi: [10.1093/mnras/stv179](https://doi.org/10.1093/mnras/stv179)

Piner, B. G., & Edwards, P. G. 2004, *The Astrophysical Journal*, 600, 115–126, doi: [10.1086/379769](https://doi.org/10.1086/379769)

Shoji, A., Fujita, Y., Kawanaka, N., Inoue, S., & Nishiwaki, K. 2025, <https://arxiv.org/abs/2507.02326>

Sironi, L., Keshet, U., & Lemoine, M. 2015, *SSRv*, 191, 519, doi: [10.1007/s11214-015-0181-8](https://doi.org/10.1007/s11214-015-0181-8)

Tavecchio, F., Ghisellini, G., Ghirlanda, G., Foschini, L., & Maraschi, L. 2010, MNRAS, 401, 1570,
doi: [10.1111/j.1365-2966.2009.15784.x](https://doi.org/10.1111/j.1365-2966.2009.15784.x)

Wang, T.-G., & Zhang, X.-G. 2003, MNRAS, 340, 793,
doi: [10.1046/j.1365-8711.2003.06336.x](https://doi.org/10.1046/j.1365-8711.2003.06336.x)

Wang, Z.-R., Xue, R., Xiong, D., et al. 2024, ApJS, 271, 10,
doi: [10.3847/1538-4365/ad168c](https://doi.org/10.3847/1538-4365/ad168c)

Willingale, R., Starling, R. L. C., Beardmore, A. P., Tanvir, N. R., & O'Brien, P. T. 2013, MNRAS, 431, 394,
doi: [10.1093/mnras/stt175](https://doi.org/10.1093/mnras/stt175)

Wolf, M. 2019, PoS, ICRC2019, 1035,
doi: [10.22323/1.358.1035](https://doi.org/10.22323/1.358.1035)

Wood, M., Caputo, R., Charles, E., et al. 2017, in International Cosmic Ray Conference, Vol. 301, 35th International Cosmic Ray Conference (ICRC2017), 824,
doi: [10.22323/1.301.0824](https://doi.org/10.22323/1.301.0824)

Xu, J.-L., Yu, N.-P., Zhu, M., et al. 2025,
<https://arxiv.org/abs/2512.16049>

Younes, G., Porquet, D., Sabra, B., et al. 2010, Astronomy and Astrophysics, 517, A33,
doi: [10.1051/0004-6361/201014371](https://doi.org/10.1051/0004-6361/201014371)

Zhang, B. T., & Murase, K. 2023, Monthly Notices of the Royal Astronomical Society, 524, 76–89,
doi: [10.1093/mnras/stad1829](https://doi.org/10.1093/mnras/stad1829)

Zhang, J., Liang, E.-W., Zhang, S.-N., & Bai, J. M. 2012, The Astrophysical Journal, 752, 157,
doi: [10.1088/0004-637x/752/2/157](https://doi.org/10.1088/0004-637x/752/2/157)